Journal of Computational Acoustics,

USE OF WAVE BOUNDARY ELEMENTS FOR ACOUSTIC COMPUTATIONS

EMMANUEL PERREY-DEBAIN
School of Engineering, University of Durham, Durham DH1 3LE, UK

JON TREVELYAN
School of Engineering, University of Durham, Durham DH1 3LE, UK

PETER BETTESS
School of Engineering, University of Durham, Durham DH1 3LE, UK

Received (to be inserted
Revised by Publisher)

Discrete methods of numerical analysis have been used successfully for decades for the solution of problems involving wave diffraction, etc. However, these methods, including the finite element and boundary element methods, can require a prohibitively large number of elements as the wavelength becomes progressively shorter. In this work, a new type of interpolation for the acoustic field is described in which the usual conventional shape functions are modified by the inclusion of a set of plane waves propagating in multiple directions. Including such a plane wave basis in a boundary element formulation has been found in the current work to be highly successful. Results are shown for a variety of classical scattering problems, and also for scattering from non convex obstacles. Notable results include a conclusion that, using this new formulation, only approximately 2.5 degrees of freedom per wavelength are required. Compared with the 8 to 10 degrees of freedom normally required for conventional boundary (and finite) elements, this shows the marked improvement in storage requirement. Moreover, the new formulation is shown to be extremely accurate. It is estimated that for 2D Helmholtz problems, and for a given computational resource, the frequency range allowed by this method is extended by a factor of three over conventional direct collocation Boundary Element Method. Recent successful developments of the current method for plane elastodynamics problems are also briefly outlined.

1. Introduction

This paper is concerned with recent developments in solving Helmholtz equation for short wave problems using integral methods. Helmholtz equation is written here for reference as follows:

$$\nabla^2\phi + k^2\phi = 0 \tag{1.1}$$

k is the wavenumber, given by $k = 2\pi/\lambda$, where λ is the wavelength. ϕ is the field variable of interest, which could be acoustic pressure, wave elevation or an electro-magnetic potential, among many other possibilities. There is considerable interest in many application

fields in the solution of equation (1.1), when the wavelength, λ is short, or the wave number, k, is large. Present finite and boundary element solutions require prohibitively large numbers of field variables for modelling such problems so that there is a limit to the upper frequency which can be considered, which is well below the range of high frequencies of practical interest. In recent years a number of developments in the Finite Element Method (FEM) community under the generic grouping of Partition of Unity Finite Element Methods (PUFEM) [1] showed an outstanding improvement of the approximation properties of the standard FEM when applied to Helmholtz equation. Although this is not the place for a complete survey, among these attempts can be noted the papers of Laghrouche and Bettess [2,3], Mayer and Mendel [4], Farhat [5] and Ortiz[6]. Essentially, instead of using the conventional finite element approximation within each element, a set of plane waves travelling in multiple directions is also included. This procedure permits inclusion of *a priori* information about the local behaviour of the solution and the number of active variables can be greatly reduced in some cases. In the domain of structural dynamic analysis, similar techniques have been developed such as the Variational Theory of Complex Rays (Ladevèze *et al.* [7]) or the Wave Based Method introduced by Desmet [8]. Other trigonometric-like bases have been considered to enrich the conventional polynomial approximation for predicting high order plate and beam bending modes (Beslin *et al.* [9], Leung *et al.* [10]).

In previous years, the use of the plane wave basis as introduced in the PUFEM [1] has been theoretically investigated by de La Bourdonnaye [11,12] under the title of Microlocal Discretization for solving scattering problems with integral equations but no numerical results were reported. The method was developed further by Perrey-Debain *et al.* [13,14], who show highly accurate results for scattering by circular and elliptical cylinders. In another paper [15], we give details of the implementation of the method, and investigate its accuracy and numerical characteristics, including the condition number of the resulting system matrices. This paper presents an outline of the method with new results regarding scattering by non convex obstacles. Finally, in the last section, we briefly show how the current method has been successfully applied for solving plane elastodynamic problems with integral equations [16].

2. Description of the method

2.1. *Integral formulation*

Consider a two dimensional obstacle Ω of smooth boundary line Γ in an infinite propagative medium. Throughout this paper, we will consider either active obstacles with radiating source v or perfectly reflecting obstacles impinged by an incident time-harmonic wave ϕ^I. By using the direct formulation via the Green second identity, equation (1.1) is reformulated into a boundary integral equation on the boundary Γ as follows ($e^{-i\omega t}$ time-dependence)

$$\phi(x) + 2\int_\Gamma \frac{\partial G(x,y)}{\partial \nu}\phi(y)d\Gamma_y = 2\phi^I(x) + 2\int_\Gamma G(x,y)\, v\, d\Gamma_y \quad , \quad x \in \Gamma\,, \tag{2.1}$$

where ν is the normal unit vector directed into the obstacle, G is the free-space Green function $G(x,y) = (i/4)\ H_0(k|x-y|)$ where H_0 is the Hankel function of the first kind of order zero and $i = \sqrt{-1}$.

2.2. *Finite element basis*

Following the classical BEM procedure [17], equation (2.1) may be integrated numerically by subdividing the boundary into elements, over each of which the unknown potential ϕ may be expressed in terms of nodal values according to conventional interpolation using Lagrangian shape functions. This requires that each element is sufficiently small, in comparison with the wavelength (say 8 to 10 nodes per wavelength for engineering accuracy). The new feature of the boundary elements presented here, and of the corresponding finite elements that have been described in the literature, is that they express the potential ϕ as a summation of M plane wave components in different directions. To do so, we first partition the boundary line Γ into N elements, $\Gamma = \bigcup \Gamma_{n=1..N}$. On each element, the potential is then approximated as

$$\phi(x) = \sum_{p=1}^{3} \sum_{l=1}^{M} N_p(\eta) e^{ik\xi_l \cdot x} \phi_{p,l}^n \quad , \quad x \in \Gamma_n \,, \tag{2.2}$$

where functions N_p stand for the standard quadratic Lagrangian polynomial:

$$N_1 = \frac{\eta}{2}(\eta - 1), \qquad N_2 = (1 - \eta^2), \qquad N_3 = \frac{\eta}{2}(1 + \eta). \tag{2.3}$$

In equation (2.2), it is understood that η is a regular parametrization of the curve Γ_n defined by

$$\Gamma_n = \{\gamma_n(\eta) : -1 \leq \eta \leq 1\}. \tag{2.4}$$

It is important to recognise now that the coefficients $\phi_{p,l}^n$ no longer represent the nodal potentials, but are now the amplitudes of the set of M plane waves associated with the shape function N_p and element Γ_n. The continuity of the potential between two adjacent elements will be satisfied if

$$\phi_{3,l}^{n-1} = \phi_{1,l}^n \quad , \quad (n,l) \in [1,N] \times [1,M], \tag{2.5}$$

(the index 0 is assimilated with index N). This continuity requirement leads to $2M$ unknowns per element and the total degree of freedom of the system is then $N_d = 2MN$. Employing an engineering terminology, the element Γ_n and the associated approximation (2.2) will be referred to as a wave boundary element. Even though M could be considered a function of p and n, the original method suggests the use of a constant number of plane wave directions M and the use of a uniformly distributed set of directions:

$$\xi_l = \left(\cos\left(\frac{2\pi l}{M}\right), \sin\left(\frac{2\pi l}{M}\right) \right). \tag{2.6}$$

We can note that the plane wave approximation (2.2) automatically contains the conventional quadratic interpolation by simply setting $M = 1$ and $\xi_1 = 0$. This feature will allow

us a comparison between the usual polynomial interpolation and the new plane wave basis as shown in Section 3.

2.3. *Element matrices and numerical integration*

In conventional collocation BEM, the system matrix is formed by collocating the integral equation (2.1) at the natural nodes of the mesh. The new type of approximation (2.2) requires the definition of some extra collocation points in order to produce a square system. These points have been originally chosen to be equally distributed in the parametric space along each element though there might be many other ways of placing these points (see Section 4.1). Now, let b be the right-hand side of (2.1) and x is a collocation point on the element $\Gamma_{n'}$ such that $x = \gamma_{n'}(\bar{\eta})$. Replacing the potential by its the plane wave approximation (2.2) into the integral formulation yields the following linear constraint for the unknown coefficients,

$$\sum_{n=1}^{N}\sum_{p=1}^{3}\sum_{l=1}^{M}\left\{N_p(\bar{\eta})e^{ik\xi_l\cdot x}\,\delta_{nn'}+2\int_{-1}^{+1}K_n(x,\eta)N_p(\eta)e^{ik\xi_l\cdot\gamma_n(\eta)}d\eta\right\}\phi_{p,l}^{n}=b(x), \tag{2.7}$$

where

$$K_n(x,\eta)=\frac{i}{4}H_1(k|x-\gamma_n(\eta)|)\frac{(x-\gamma_n(\eta))\cdot\nu}{|x-\gamma_n(\eta)|}\left|\frac{d\gamma_n}{d\eta}\right|, \tag{2.8}$$

H_1 is the Hankel function of the first kind of order one and δ denotes the Kronecker symbol. Collocating (2.7) at N_d points yields the following matrix system

$$\boldsymbol{A}\boldsymbol{\phi}=(\boldsymbol{W}+\boldsymbol{K})\boldsymbol{\phi}=\boldsymbol{b}\,, \tag{2.9}$$

where the vector $\boldsymbol{\phi}$ contains the plane wave coefficients. The sparse matrix $\boldsymbol{W}$ stemming from the first term of (2.7) can be interpreted as the plane wave interpolation matrix for the potential ϕ, $\boldsymbol{K}$ is the boundary element matrix stemming from integrals of (2.7) and $\boldsymbol{b}$ is the source vector containing either the incident wave or the radiating term. This latter contains a logarithmic singularity that can be easily removed by using the cubic Telles' transformation [18]. At this stage, it is worth noticing that the finite element basis (2.2) allows a significantly increased element size as each element can contain many wavelengths and conventional integration schemes [17] are not appropriate. In order to produce element matrices at any desired accuracy whatever the element length, we consider a regular subdivision of the interval $[-1,+1]$ and use 10 Gauss points over each subdivision. This procedure is very effective as long as the integrand in the parametric space $f(\eta)$ has good regularity properties which is not the case when a collocation point belongs to the element to be integrated. In this latter case, the integration scheme can be written as follows

$$\int_{-1}^{1}f(\eta)d\eta=\int_{-1}^{\bar{\eta}}f(\eta)d\eta+\int_{\bar{\eta}}^{1}f(\eta)d\eta, \tag{2.10}$$

where $\bar{\eta}$ is the local coordinate of the collocation point. These two integrals are then integrated using the same procedure as for the regular case. All operations are performed with double precision and the Green's function and its normal derivative are evaluated using the routines for Bessel functions of fractional order (as recommended) from Numerical Recipes[19].

2.4. *Singular Value Decomposition and instabilities*

Two sources of numerical instabilities are likely to spoil the solution of (2.9) if a direct solver is used. The first one stems from the non invertibility of the integral operator (2.1) when k is an eigenfrequency of the corresponding interior Dirichlet problem [20]. In order to alleviate this non-uniqueness problem difficulty, we add some extra equations by collocating the internal Helmholtz integral equation at so-called CHIEF points located inside the obstacle [21]. The second stems from the intrinsic nature of the plane wave approximation. These instabilities are usually manifested in matrices with very high condition numbers and are somewhat similar to those encountered when using source simulation techniques [22,23]. In previous research, it has been observed that the condition number grows very rapidly as the number of plane waves becomes large or as the frequency decreases [3,13]. We give an explanation of this behaviour in [15]: the condition number is mainly governed by the number of collocation points or samples per wavelength, α, and the number M of directions in the plane wave basis. To illustrate our matter, we consider the regular discretization of the circular cylinder of radius a with N elements:

$$\Gamma_n = \left\{ \gamma_n(\theta) = a(\cos\theta, \sin\theta) \quad , \quad \theta = \frac{\pi}{N}(2n - 1 + \eta) \quad , \quad \eta \in [-1, +1] \right\}. \tag{2.11}$$

The number of plane waves M is chosen accordingly so that the total number of variables is kept constant $N_d = 2NM = 64$. To cope with finite precision and inaccuracies of the element matrices, we denote the computed version of the quantity $\boldsymbol{X}$ by $\hat{\boldsymbol{X}} = \boldsymbol{X} + \Delta\boldsymbol{X}$. The Singular Value Decomposition (SVD) of the overdetermined system matrix $\hat{\boldsymbol{A}}$ is performed by the real SVD solver from Numerical Recipes [19] for which the complex matrix coefficients have been previously transformed into real data by means of the following replacements:

$$\hat{a}_{ij} \quad \rightarrow \quad \begin{pmatrix} \mathrm{Re}(\hat{a}_{ij}) & -\mathrm{Im}(\hat{a}_{ij}) \\ \mathrm{Im}(\hat{a}_{ij}) & \mathrm{Re}(\hat{a}_{ij}) \end{pmatrix}. \tag{2.12}$$

The 2-norm condition number of $\hat{\boldsymbol{A}}$ is numerically evaluated as $\hat{\kappa}_2(\hat{\boldsymbol{A}}) = \hat{\sigma}_1/\hat{\sigma}_{N_d}$ where $\hat{\sigma}_1$ and $\hat{\sigma}_{N_d}$ denote respectively the largest and smallest singular value. We define the number of degrees of freedom (or equivalently the number of collocation points) per wavelength, α by

$$\alpha = \frac{N_d \lambda}{P}, \tag{2.13}$$

where P is the perimeter of Γ. This parameter is a useful measure of the efficiency of the method. The influence of α and M on the conditioning effects are clearly illustrated in

Figure 1. As the number of plane waves M increases, the condition number grows very rapidly with respect to α and this behaviour has been observed for other obstacles. The condition number will also increase moderately with the system dimension but its behaviour with respect to α and M remains similar.

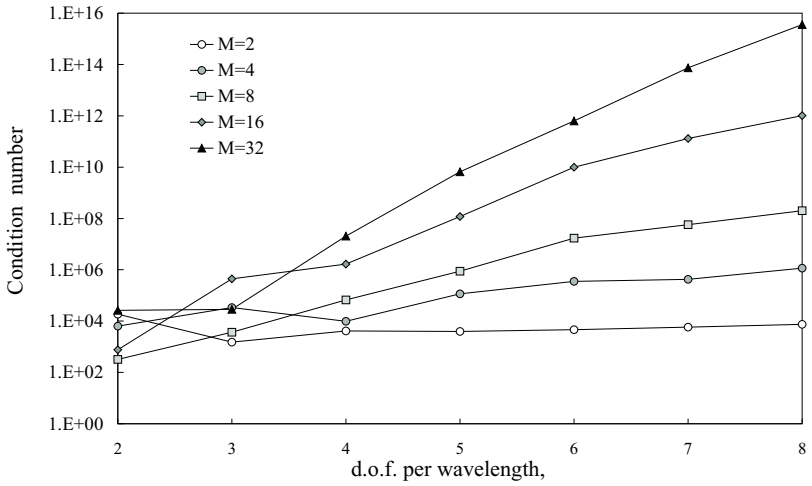

Fig. 1. Condition number as a function of the number of directions M and α.

The condition number provides a measure of the calculational stability and high condition numbers generally yield vector solutions $\boldsymbol{\phi}$ with high norm (few orders of magnitude) which are likely to be corrupted by round-off errors. Curiously enough, this is not necessarily a major problem and good solutions for ϕ recovered after recombination in (2.2) can still be obtained provided that the matrix coefficients have been computed with sufficient accuracy. In any cases, however, very small singular values will certainly reflect inaccuracies of $\hat{\boldsymbol{A}}$ and best results have been obtained by discarding singular values below $10^{-12}\hat{\sigma}_1$. In the following sections, all numerical experiments have been carried out using this truncation.

3. Error analysis for simple configurations

3.1. *A radiating problem*

As a first test case, we consider the pulsating circular cylinder problem with $v = 1$. The analytical solution is independent of θ and is given by

$$\tilde{\phi}|_\Gamma = \frac{H_0(ka)}{(kH_1(ka))}. \tag{3.1}$$

The discretization is strictly the same as the one of the previous section and 10 CHIEF points are added to alleviate the non-uniquenes problem. The quality of the solution is

controlled by the relative L_2 error defined as

$$E_2 = \frac{\|\phi - \tilde{\phi}\|_{L_2(\Gamma)}}{\|\tilde{\phi}\|_{L_2(\Gamma)}}, \tag{3.2}$$

where ϕ and $\tilde{\phi}$ denote the computed and exact solutions respectively. Table 1 compares errors obtained for three configurations in the range of frequencies $ka \in [0, 50]$. The total number of variables is kept constant, $N_d = 128$. An interesting result is the ability of the plane wave basis to represent a constant profile with 9 to 10 exact figures. These results are somewhat similar to the corresponding scattering problem [14] and best results are obtained by considering large elements with many directions.

3.2. *Scattering problems*

In this section, we shall present some results for the scattering of an incident plane wave $\phi^I(x) = e^{ikd\cdot x}$ propagating along the horizontal direction $d = (1, 0)$ by a hard circular cylinder of radius a. In polar coordinates, the field can be represented by separable solutions and the exact scattered potential is given by the infinite series [24]:

$$\tilde{\phi}^S(x) = -\frac{J_0'(ka)}{H_0'(ka)} H_0(kr) - 2\sum_{n=1}^{\infty} i^n \frac{J_n'(ka)}{H_n'(ka)} H_n(kr)\cos n\theta\,, \tag{3.3}$$

where $x = r\,(\cos\theta, \sin\theta)$, $H_n(kr)$ and $J_n(kr)$ are, respectively, Hankel and Bessel functions of the first kind and order n, and the prime denotes differentiation with respect to kr. This series is well-behaved and allows us to produce very accurate results without deterioration at high frequency.

In Table 2 are displayed errors obtained with $M = 32$ directions for a large frequency range. The associated condition numbers are also presented. The number of wave boundary elements is chosen according to (2.13) so that $\alpha = 2.5$. The last two columns show results obtained by using the quadratic approximation with $\alpha = 10$ and the associated number of conventional elements. In all cases we used 30 CHIEF equations. At low frequency (say $ka < 50$), 2.5 degrees of freedom per wavelength seems too low to obtain a satisfying solution. Results are much more accurate at higher frequencies and this is in agreement

Table 1. Relative L_2 errors (%) for the pulsating circular cylinder.

ka	$N = 8$, $M = 8$	$N = 4$, $M = 16$	$N = 2$, $M = 32$
10	$2.2\,10^{-7}$	$3.1\,10^{-8}$	$2.2\,10^{-8}$
20	$1.3\,10^{-3}$	$1.0\,10^{-6}$	$2.5\,10^{-7}$
30	$3.0\,10^{-3}$	$3.2\,10^{-5}$	$5.3\,10^{-6}$
40	$2.6\,10^{-1}$	$8.9\,10^{-1}$	$1.3\,10^{-2}$
50	23.0	4.2	1.14

with the high frequency approximation properties of the the plane wave basis (see de La Bourdonnaye [12]). Clearly, the accuracies and economies over conventional approximation are very substantial for this frequency range. Because α and M are kept fixed, the condition number grows moderately with respect to the system dimension and the truncation is not active here. We can observe that these wave elements contains approximately $2M/\alpha \approx 26$ oscillations.

At sufficiently high frequency and at least for rigid convex objects, it is known that the distribution on the illuminated part of the scatterer can be determined on the assumption that at every point the incident wave is reflected as if it were impinging on the infinite tangent plane [24]. This approximation, known as physical optics, assumes that the secondary field stemming from the integral on the left-hand side of (2.1) can be disregarded in comparison with the incident wave. Thus, $\phi \sim 2\phi^I$ on the illuminated zone. For this reason, the last results are optimum in the sense that one of the directions of the plane wave set, see (2.6), actually coincides with the horizontal direction of the incident wave. The influence of the angular origin of the distribution (2.6) can be conveniently described by considering the new rotated set $\xi_{l+\delta}$ with $0 \leq \delta \leq 1$. Figure 2 shows the influence of δ for 4 configurations at $k = 100$. It is rather strong since one to two orders of magnitude variation in error can be observed for any (M, N) displayed. The very poor results obtained for the cases $[M = 16, N = 8, 0.2 \leq \delta \leq 0.8]$ are simply due to an insufficient number of degrees of freedom per wavelength ($\alpha = 2.55$). Indeed, by taking 10 wave elements ($\alpha = 3.2$), all errors are found below 0.15%. As expected, the best result is 0.002% when $\delta = 0, 1$.

We consider the scattering of an incident plane wave propagating along the direction $d = (\cos\theta^I, \sin\theta^I)$ with $\theta^I = 60^\circ$ by a hard elliptical cylinder of semi-major axis a (resp. semi-minor axis b). The analytical solution for the scattered field can be developed in terms of Mathieu functions and is given in Jones [24]. We investigated the quality of the solution ϕ for a relatively large range of aspect ratios ($0.5 \geq b/a \geq 0.01$). Results of Table 3 shows L_2 relative errors for the two cases:

(i) 1 wave element with $M = 24$ at $ka = 20$,
(ii) 1 wave element with $M = 48$ at $ka = 40$.

Table 2. Relative L_2 errors for scattering by a hard circular cylinder.

ka	Rel. L_2 err.(%) $M = 32$, $\alpha = 2.5$	Number of wave elts	C.N. $(\log_{10}(\hat{\kappa}_2(\hat{\boldsymbol{A}})))$ $M = 32$, $\alpha = 2.5$	Rel. L_2 err.(%) Quad., $\alpha = 10$	Number of quad. elts
25.6	11.7	1	4.1	0.68	128
51.2	1.68	2	4.2	0.65	256
76.8	0.47	3	4.6	0.74	384
128.0	0.05	5	5.6	0.65	640
256.0	0.02	10	6.5	not available	-
384.0	0.14	15	7.1	not available	-
512.0	0.68	20	8.0	not available	-

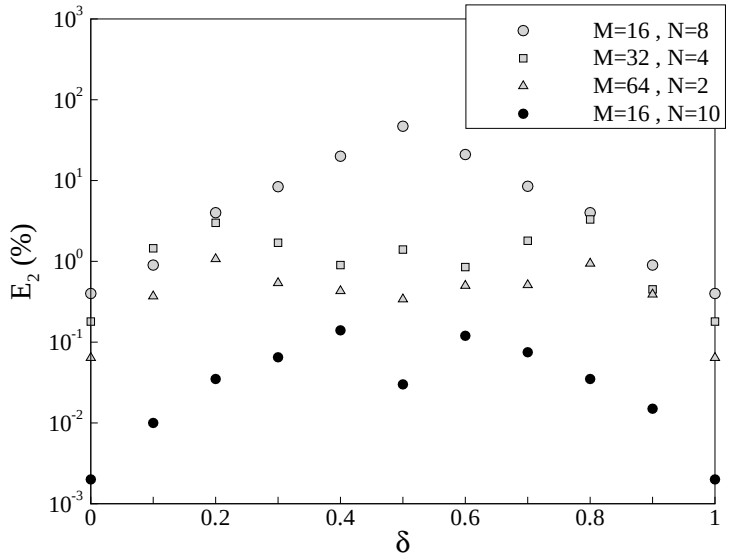

Fig. 2. Influence of the angular origin on the errors for the scattering of a plane wave, $k = 100$.

Note that in both cases, the incident direction is considered in the set. The decrease of the errors with respect to the aspect ratio is simply due to the increase of the parameter α whose value is reported in the last column. The striking improvement between these two tests stems from a better approximation of the plane wave basis as the number of directions M increases. In Figure 3 are plotted the computed and analytical potentials on the single wave element. This shows the global approximation properties of the plane wave basis as well as the ability to handle corners with very small radius of curvature.

4. Efficiency of the method for non convex scatterers

Results from Table 2 concerning the scattering by a hard circular cylinder are certainly

Table 3. Relative L_2 errors (%) for scattering by a hard elliptical cylinder. Only 1 wave element is used.

b/a	$M = 24, ka = 20$	$M = 48, ka = 40$	α
0.50	1.20	0.03	3.11
0.20	0.43	0.0007	3.58
0.10	0.09	0.0008	3.71
0.05	0.05	0.00005	3.75
0.02	0.05	0.00006	3.76
0.01	0.05	0.00008	3.76

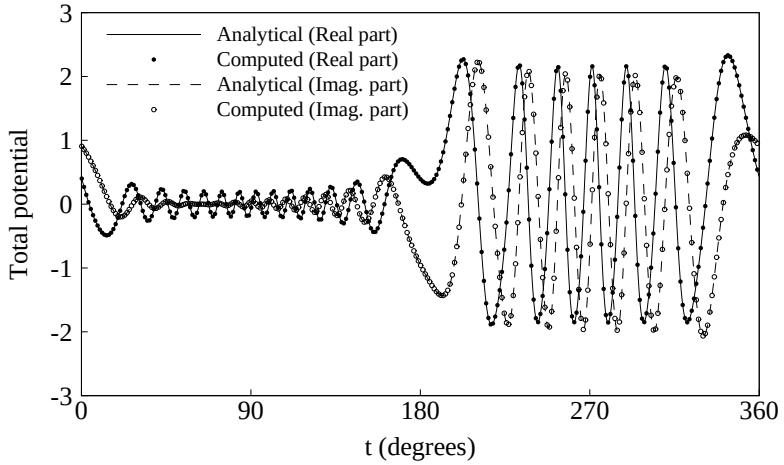

Fig. 3. Potential along the ellipse, $b/a = 0.01$, $\theta^i = 60^\circ$ and $ka = 40$.

giving the best efficiency one would expect from the current method. The purpose of this section is to test the efficiency of the plane wave basis when dealing with scattering by non convex objects.

4.1. *The boomerang-shaped obstacle*

The profile of the scatterer is illustrated in Figure 4 and is described by the parametrization

$$\gamma(\theta) = ([\cos\theta + 10\cos 2\theta - 10]/10,\ \sin\theta) \quad , \quad 0 \leq \theta \leq 2\pi. \tag{4.1}$$

For the purpose of simplification, we will refer to the parameter t in degrees: $t = (180/\pi)\theta$. The two smooth sharp corners with very small radius of curvature are located at $t = 90^\circ$ (top corner) and $t = 270^\circ$ (bottom corner). In this example, we are interested in the scattering of a unit incident plane wave with direction 45° at $k = 30$. 4 configurations have been tested and results are summarized in Table 4 and in Figure 5. Two sampling schemes have been investigated (see Figure 4):

(i) a regular sampling in the parametric space that automatically concentrates the collocation points at the corners,
(ii) a regular sampling in the real space where the distance along the boundary line between two collocation points is kept constant.

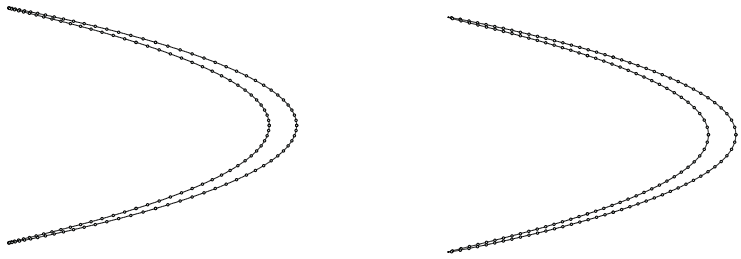

Fig. 4. Location of the of the collocation points on the boomerang-shaped obstacle. Left: regular sampling in the parametric space. Right: regular sampling in the real space.

The three first configurations gave good results whose differences are not distinguishable on the plot and are therefore refered to a single curve labelled A. The last configuration gave poor results (curve B). This shows that more information is needed near the sharp corners than on the flat region of the boundary line and a regular sampling in the real space is likely to diminish the efficiency. The 2D isoline picture of the absolute value of total field around the scatterer is shown in Figure 6. Care was taken to ensure that values of the potential in the vicinity of the boundary are computed with sufficient accuracy to take into account the $O(1/r)$ behaviour of the normal derivative of the Green's function.

4.2. *The star-shaped obstacle*

The profile of the scatterer is illustrated in Figure 6 and is described by the parametrization

$$\gamma(\theta) = [1 + 0.5\cos 10\theta]\,(\cos\theta,\, \sin\theta) \quad , \quad 0 \leq \theta \leq 2\pi. \tag{4.2}$$

We are interested in the scattering of two unit incident plane waves of direction 0° and 90° at $k = 30$. Results are plotted in Figure 7. The curve $[N = 6, M = 32]$ can be considered as the exact solution and the associated efficiency is $\alpha = 3.7$. The case $[N = 5, M = 32]$ gives satisfying results of engineering accuracy and the efficiency is $\alpha = 3.1$. Surprisingly, the plane wave approximation does not seem to be affected by this rather difficult test and the efficiency remains very satisfactory.

Table 4. 4 configurations for the boomerang-shaped obstacle.

Configuration	Regular sampling	Solution	Curve (Fig.5)	α
$N = 4$, $M = 18$	parametric space	good	A	3.2
$N = 3$, $M = 24$	parametric space	good	A	3.2
$N = 4$, $M = 24$	real space	good	A	4.2
$N = 4$, $M = 18$	real space	bad	B	3.2

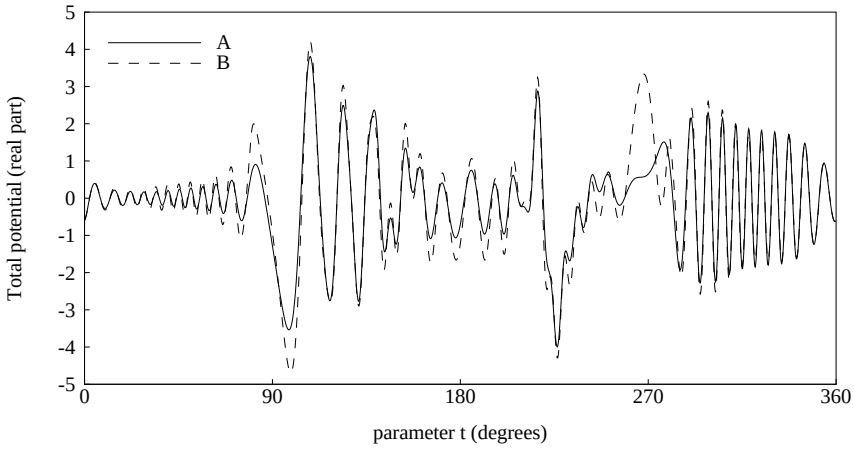

Fig. 5. Potential on the boundary of boomerang-shaped obstacle due the scattering of a unit incident plane wave of direction 45° at $k = 30$.

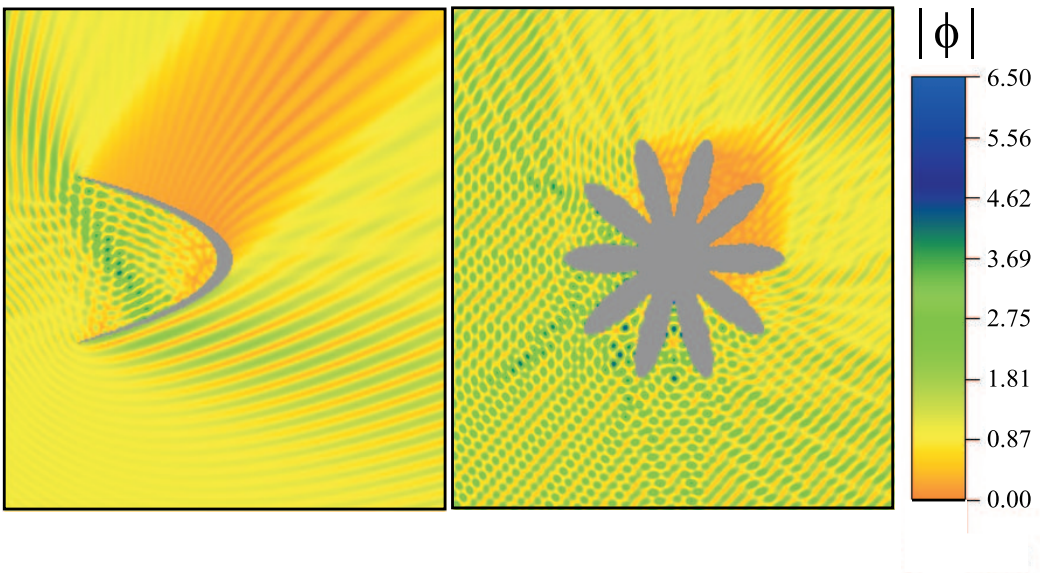

Fig. 6. Total field (abs. value) around the scatterer. Left: the boomerang-shaped obstacle ($\theta^I = 45°$ at $k = 30$). Right: the star-shaped obstacle ($\theta_1^I = 0°$ and $\theta_2^I = 90°$ at $k = 30$)

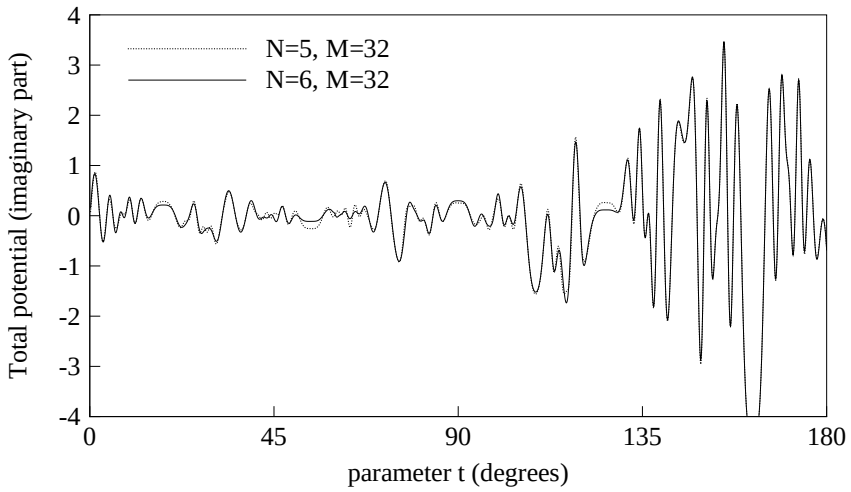

Fig. 7. Potential on the boundary of the star-shaped obstacle due the scattering of two unit incident plane waves of direction 0° and 90° at $k = 30$.

4.3. *The submarine*

As a final test, we adapt the plane wave basis for engineering applications such as the scattering by an idealised bidimensional obstacle of submarine shaped section, of length $L = 18$ and mean diameter $D = 2.5$ (Figure 8). The boundary line of the scatterer is composed of straight lines and arcs of circles. The smooth corners are portions of circles with radius $1/10$. These simple curves are assembled such that the Jacobian of the transformation is kept constant along the boundary line. This ensures the proportionality between the length of the curve and the circular parameter θ as

$$\int_0^\theta \left| \frac{d\gamma}{d\theta'} \right| d\theta' = \frac{P}{2\pi}\theta\,, \tag{4.3}$$

where P is the perimeter of the scatterer.

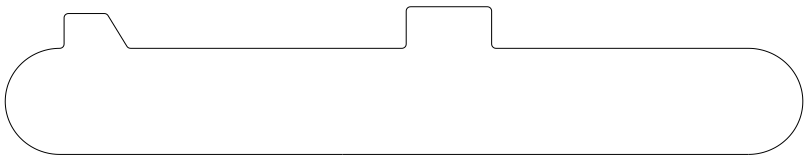

Fig. 8. Submarine shape.

Three high-frequency tests has been carried out and results are summarized in Table 5. We can note that the linear relation (4.3) automatically provides a regular discretization of the scatterer and a regular distribution of collocation points along the boundary line. The matrix solver used here is an optimised QR decomposition from the Compaq Extended Math Library (CXML) which have been shown to be much more efficient than the SVD solver. The penultimate column shows the Root Mean Square value of the plane wave coefficients. These values can be much higher than the norm of the physical solution ϕ recovered after recombination in (2.2). This stems from round-off errors associated with small singular values which have not been discarded. Fortunately, their effects are rather mild as long as the matrix coefficients are computed with sufficient accuracy (in practice, about 40 integration points per wavelength is recommended). The last row gives the total CPU time, which is mostly consumed for the computation of the system matrix, the time for solving the system (in brackets) being only 3 minutes for the last case ($k = 120$). An acceleration of the integration procedure is a subject of further investigation and it is believed that the CPU time could be reduced by an order of magnitude.

Scattering results are conveniently illustrated on Figure 9 where the far-field pattern (in decibels) has been plotted for the case: $k = 40$ and $\theta^I = 215°$. The far-field pattern ϕ_∞ is defined by the asymptotic behavior of the scattered wave $\phi^S(x) = e^{ik|x|}|x|^{-1/2}\phi_\infty(\hat{x}) + O(|x|^{-3/2})$ as $|x| \to \infty$, uniformly for all directions $\hat{x} = x/|x|$ and is given by

$$\phi_\infty(\hat{x}) = \sqrt{\frac{k}{8\pi}} e^{-i\pi/4} \int_\Gamma \hat{x} \cdot \nu(y) e^{-ik\hat{x}\cdot y} \phi(y) d\Gamma_y. \tag{4.4}$$

Discrete values of (4.4) have been computed on a fine resolution with 20 evaluation points per degree. The secondary peak located at 145° stems from the reflection of the incident field from the top surface of the submarine. A zoom of the primary peak is also shown.

5. Application for plane elastodynamic problems

The success of the plane wave approximation for Helmholtz problems led us to ask whether such a representation of the unknown function could also succeed for elastic waves. Let us consider the scattering of an incident elastic wave u^I by a bidimensional cavity Ω of smooth boundary line Γ. Using the Somigliana identity, the boundary value problem can be written as [25]

$$u(x) + 2\int_\Gamma T(x,y)u(y)\, d\Gamma_y = 2u^I(x) \quad , \quad x \in \Gamma, \tag{5.1}$$

Table 5. Scattering by submarine, (all calculations are performed on a single-processor 2 GHz Pentium IV).

k	θ^I	L/λ	N	M	α	ϕ_{rms}	Time (QR CXML)
40	215°	115	4	100	2.95	$9.0\ 10^1$	16 min (6 s)
80	345°	230	8	100	2.95	$1.4\ 10^2$	2 h 23 min (50 s)
120	45°	345	12	100	2.95	$1.8\ 10^3$	8 h 58 min (3 min)

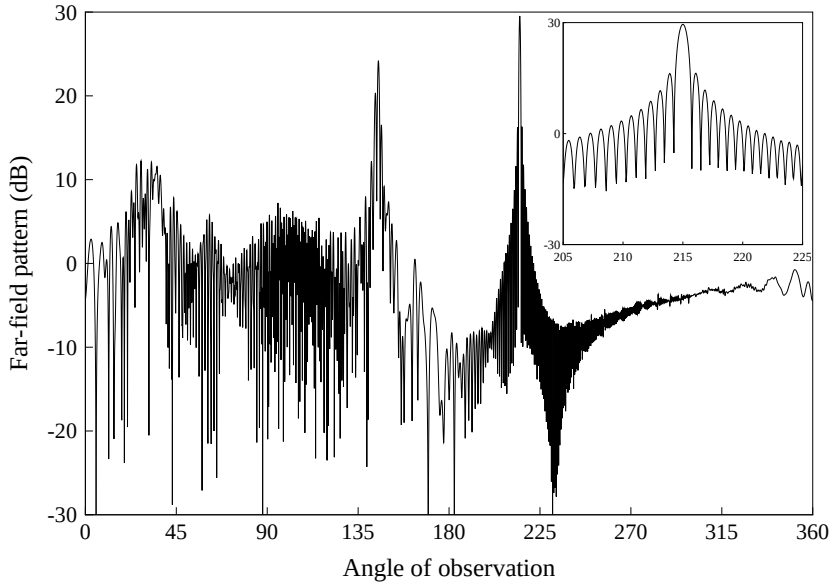

Fig. 9. Far-field pattern plot for the submarine, $\theta^I = 215^\circ$ at $k = 40$.

where the integral is taken in the sense of the Cauchy principal value. T is the Stokes' traction tensor which describes the dynamical stress field at y due to a time-harmonic point force at x at frequency ω. We denote using k_p the compressional wave number and k_s the shear wave number associated with (5.1). The link between the vector field u and the potential ϕ of the previous section becomes clear when considering the Helmholtz decomposition for the displacement field [26], namely

$$u = \nabla\phi_p + \nabla^\perp\phi_s\,, \tag{5.2}$$

where the Lamé potentials ϕ_p (resp. ϕ_s) are solutions of the Helmholtz equation with wave number k_p (resp. k_s). Now, we consider a plane wave basis of the type (2.2) for ϕ_p with M_p directions and similarly for ϕ_s with M_s directions. By introducing these two plane wave approximations in (5.2) and keeping the leading order terms (i.e. k_p and k_s sufficiently high) leads to the following representation using a set of P-waves and S-waves as

$$u(x) = \sum_{p=1}^{3} N_p(\eta) \left\{ \sum_{l=1}^{M_p} u^p_{p,l,n}\, \xi_l\, e^{ik_p\, \xi_l \cdot x} + \sum_{l=1}^{M_s} u^s_{p,l,n}\, \zeta_l^\perp\, e^{ik_s\, \zeta_l \cdot x} \right\} \quad , \quad x \in \Gamma_n\,, \tag{5.3}$$

where directions ξ_l and ζ_l have been chosen to be evenly distributed on the unit circle. The terms $u^p_{p,l,n}$ and $u^s_{p,l,n}$ no longer represent the value of the displacement, but are instead the amplitudes of the set of P-waves and S-waves. Here again, the approximation (5.3) can be easily transformed to the conventional quadratic interpolation. It suffices to set

$M_p = M_s = 1$ and consider the basis

$$u(x) = \sum_{e=1}^{3} N_e(\eta)\{u^p_{e,1,n} e_1 + u^s_{e,1,n} e_2\} \quad , \quad x \in \Gamma_n \,, \tag{5.4}$$

where e_1 and e_2 form the natural Cartesian basis of the plane. This last expression is a quadratic approximation and for this particular case, coefficients $u^p_{e,1,n}$ and $u^s_{e,1,n}$ stand respectively for the horizontal and the vertical component of the displacement field u associated with node e on element Γ_n.

The algebraic system is obtained by collocating (5.1) at some points regularly distributed on the boundary Γ. Futhermore, the condition of zero displacement at points of the internal domain is used in order to cancel the non-uniqueness problem [21]. The Cauchy principal value of singular integrals involved in (5.1) are performed using the procedure developed by Guiggiani and Casalini [27]. All operations are performed with double precision and the Stokes' traction tensor terms are evaluated using the routines for Bessel functions of fractional order from [19]. In order to keep a good accuracy when computing these terms for a very small argument (typically $k_s|x-y| < 10^{-4}$), asymptotic formulas derived from the series expansion given in [28] are used. The overdetermined system then is solved by a standard Singular Value Decomposition routine and small singular values below $10^{-12}\hat{\sigma}_1$ are discarded in order to avoid round-off errors and to achieve a better accuracy.

We shall present some results concerning the scattering of a S-wave travelling from the left to the right along the horizontal direction $u^I(x) = -e_2 e^{ik_s\, e_1 \cdot x}$ impinging a circular cavity of radius a. In all cases, the compressional wave number is chosen accordingly such that $k_s/k_p = 2$ which is a common value for a wide range of materials. This problem has an analytical solution that can be found in [29]. The boundary discretization is perfectly regular and we consider two configurations:

(i) 3 wave elements with $M_p = 24$ and $M_s = 48$,
(ii) 108 conventional quadratic elements.

The number of degrees of freedom used for both methods is $N_d = 432$. The efficiency of the wave element is clearly illustrated in Table 6 where relative L_2 errors are computed at

Table 6. Relative L_2 errors (%) for the scattering of a S-wave by a circular cavity.

$k_s a$	Wave element	Quadratic element	d.o.f. per wavelength
10	$8\ 10^{-7}$	0.1	21.6
20	$4\ 10^{-6}$	1.1	10.8
30	$2\ 10^{-5}$	6.1	7.2
50	$9\ 10^{-5}$	47	4.3
70	$4\ 10^{-2}$	81	3.1
80	2.4	95	2.7

different frequencies. In the last column is reported the associated degree of freedom per wavelength (we consider the smallest wavelength: $2\pi/k_s$). The striking result is that the new wave elements have errors between 4 and 5 orders of magnitude smaller than those of the conventional elements. Moreover, they extend the useful frequency range up to 4 times. In this example, the efficiency of the method both in terms of accuracy and computational savings is very similar to the Helmholtz problem.

6. Conclusion

A new type of boundary element called wave element has been presented. The method involves the use of plane waves to multiply the boundary element shape functions. Accurate results have been demonstrated for classical scattering problems. In practical terms, the results of this work show that, for any given amount of computational resource, these wave boundary elements enable the supported frequency range to be extended by a factor of 3 to 4 over conventional, direct collocation boundary elements for two-dimensional cases. The method may be expected to show even greater improvements in frequency range for three-dimensional analysis. Since this addresses the single most important factor limiting the use of discrete numerical methods in analysis of wave problems, this advance is expected to have a significant impact on a wide variety of engineering simulations.

Acknowledgments

This work has been funded by the EPSRC, under grant GR/N09879. We are very grateful to EPSRC for this support for Dr. Emmanuel Perrey-Debain. Peter Bettess is also grateful to the EPSRC Senior Research Fellowship committee, chaired by Professor Sir Richard Brook, which is funding this work, through EPSRC Grant Number: SF/000169. We are grateful to BAE SYSTEMS and particularly Dr. David Rowse and Dr. Simon Benham for their support and interest. We are also grateful to Dr. Omar Laghrouche and Rie Sugimoto for useful discussions.

References

1. J.M. Melenk, and I. Babuška, *Int. J. Num. Meth. Eng.*, **40**, 727 (1997).
2. O. Laghrouche and P. Bettess, *J. Comp. Acou.*, **8**(1), 189 (2000).
3. O. Laghrouche, P. Bettess and R.J. Astley, *Int. J. Num. Meth. Eng.*, **54**, 1501 (2002).
4. P. Mayer and J. Mendel, "The Finite Ray Element Method for the Helmholtz equation of scattering: first numerical experiments," UCD/CCM Report 111, (1997). URL: http://www-math.cudenver.edu/ccm/reports.html
5. C. Farhat, I. Harari and L. Franca , "The Discontinous Enrichment Method," Report Number CU-CAS-00-20, College of Engineering, University of Colorado, Boulder, Colorado, U.S.A., (2000).
6. P. Ortiz and E. Sanchez, *Int. J. Num. Meth. Eng.,* **50**, 2727 (2000).
7. P. Ladevèze, L. Arnaud, P. Rouch and C. Blanzé, *Eng. Comp.,* **18** (1/2), 193 (2001).
8. W. Desmet, " A Wave Based Prediction Technique for Coupled Vibro-Acoustic Analysis," Ph.D. Thesis, KU Leuven, division PMA, (1998).
9. O. Beslin and J. Nicolas, *J. Sound and Vib.,* **202**(5), 633 (1997).

10. A.Y.T. Leung and J.K.W. Chan, *J. Sound and Vib.,* **212**(1), 179 (1998).
11. A. de La Bourdonnaye, *C. R. A. S.*, Paris, Série I, **318**, 385 (1994).
12. A. de La Bourdonnaye, *C. R. A. S.*, Paris, Série I, **318**, 765 (1994).
13. E. Perrey-Debain, J. Trevelyan and P. Bettess, *Comm. Num. Meth. Eng.*, **18** (4), 259 (2002).
14. E. Perrey-Debain, J. Trevelyan and P. Bettess, "Using wave boundary elements in BEM for high frequency scattering," *Proceedings of the 3rd UK Conference on Boundary Integral Methods,* ed. P.J. Harris (University of Brighton Press, 2001), pp. 119 - 128.
15. E. Perrey-Debain, J. Trevelyan and P. Bettess, to appear in *J. Sound and Vib.*
16. E. Perrey-Debain, J. Trevelyan and P. Bettess, "P-wave and S-wave boundary elements for scattering of elastic waves," *Proc. 10th Annual Conference of the ACME,* eds. J. Bonet, R.H. Ransing and S. Slijepcevic (Faculty of Engineering, University of Wales, Swansea, 2002), pp. 103 - 106.
17. R.D. Ciskowski and C.A. Brebbia, *Boundary Element Methods in Acoustics*, (Computational Mechanics Publications/Elsevier Applied Science, Southampton Boston/London New York, 1991).
18. J.C.F. Telles, *Int. J. Num. Meth. Eng.*, **24**, 959 (1987).
19. W.H. Press, A.A. Teukolsky, W.T. Vetterling and B.P. Flannery, *Numerical Recipes in Fortran,* (Cambridge University Press, 1992).
20. S. Amini and M. Kirkup, *J. Comp. Phys.*, **118**, 208 (1995).
21. H.A. Schenck, *J. Acoust. Soc. Am.*, **44**, 41 (1968).
22. W. Tobocman, *J. Acoust. Soc. Am.*, **77** (2), 369 (1985).
23. M. Ochmann, *J. Acoust. Soc. Am.*, **105** (5), 2574 (1999).
24. D.S. Jones, *Acoustic and Electromagnetic Waves*, (Clarendon Press, Oxford, 1986).
25. J. Dominguez, *Boundary Elements in Dynamics*, (Computational Mechanics Publications, 1993).
26. J.D. Achenbach, *Wave Propagation in Elastic Solids*, (Elsevier Science Publisher B.V., Amsterdam, 1984).
27. M. Guiggiani, P. Casalini, *Int. J. Num. Meth. Eng.* **24**, 1711 (1987).
28. M. Abramovitz, I.A. Stegun, *Handbook of Mathematical Functions*, (Vol. 55 of Appl. Math. Ser., 10th edition, National Bureau of Standards, U.S. Governement Printing Office, Washington, D.C., 1972).
29. Y. Pao, *Trans. ASME, Ser. E - J. Appl. Mech.*, **29** (2), 299 (1962).